

# CELLULAR AUTOMATA IN MATERIALS SCIENCE WITH PARTICULAR REFERENCE TO RECRYSTALLIZATION SIMULATION

---

Dierk Raabe

*Max-Planck-Institut für Eisenforschung, Max-Planck-Str. 1, 40237 Düsseldorf, Germany,  
e-mail: raabe@mpie.de*

**Key Words** integrated model, interface, transformation, nucleation, crystal plasticity

■ **Abstract** The paper is about cellular automaton models in materials science. It gives an introduction to the fundamentals of cellular automata and reviews applications, particularly for those that predict recrystallization phenomena. Cellular automata for recrystallization are typically discrete in time, physical space, and orientation space and often use quantities such as dislocation density and crystal orientation as state variables. Cellular automata can be defined on a regular or nonregular two- or three-dimensional lattice considering the first, second, and third neighbor shell for the calculation of the local driving forces. The kinetic transformation rules are usually formulated to map a linearized symmetric rate equation for sharp grain boundary segment motion. While deterministic cellular automata directly perform cell switches by sweeping the corresponding set of neighbor cells in accord with the underlying rate equation, probabilistic cellular automata calculate the switching probability of each lattice point and make the actual decision about a switching event by evaluating the local switching probability using a Monte Carlo step. Switches in a cellular automaton algorithm generally performed as a function of the previous state of a lattice point and the state of the neighboring lattice points. The transformation rules can be scaled in terms of time and space using, for instance, the ratio of the local and the maximum possible grain boundary mobility, the local crystallographic texture, the ratio of the local and the maximum-occurring driving forces, or appropriate scaling measures derived from a real initial specimen. The cell state update in a cellular automaton is made in synchrony for all cells. The review deals, in particular, with the prediction of the kinetics, microstructure, and texture of recrystallization. Couplings between cellular automata and crystal plasticity finite element models are also discussed.

## INTRODUCTION TO CELLULAR AUTOMATA

### Basic Setup of Cellular Automata

Cellular automata are algorithms that describe the discrete spatial and temporal evolution of complex systems by applying local (or sometimes long-range)

deterministic or probabilistic transformation rules to the cells of a regular (or nonregular) lattice.

The space variable in cellular automata usually stands for real space, but orientation space, momentum space, or wave vector space can be used as well. Cellular automata can have arbitrary dimensions. Space is defined on a regular array of lattice points that can be regarded as the nodes of a finite difference field. The lattice maps the elementary system entities that are regarded as relevant to the model under investigation. The individual lattice points can represent continuum volume units, atomic particles, lattice defects, or colors depending on the underlying model. The state of each lattice point is characterized in terms of a set of generalized state variables. These could be dimensionless numbers, particle densities, lattice defect quantities, crystal orientation, particle velocity, blood pressure, animal species, or any other quantity the model requires. The actual values of these state variables are defined at each of the individual lattice points. Each point assumes one out of a finite set of possible discrete states. The opening state of the automaton, which can be derived from experiment (for instance from a microtexture experiment) or theory (for instance from crystal plasticity finite element simulations), is defined by mapping the initial distribution of the values of the chosen state variables onto the lattice.

The dynamical evolution of the automaton takes place through the application of deterministic or probabilistic transformation rules (also referred to as switching rules) that act on the state of each lattice point. These rules determine the state of a lattice point as a function of its previous state and the state of the neighboring sites. The number, arrangement, and range of the neighbor sites used by the transformation rule for calculating a state switch determine the range of the interaction and the local shape of the areas that evolve. Cellular automata work in discrete time steps. After each time interval, the values of the state variables are updated for all lattice points in synchrony, mapping the new (or unchanged) values assigned to them through the transformation rule.

Owing to these features, cellular automata provide a discrete method of simulating the evolution of complex dynamical systems that contain large numbers of similar components on the basis of their local (or long-range) interactions. Cellular automata do not have restrictions in the type of elementary entities or transformation rules employed. They can map such different situations as the distribution of the values of state variables in a simple finite difference simulation, the colors in a blending algorithm, the elements of fuzzy sets, or elementary growth and decay processes of cells. For instance, the Pascal triangle, which can be used to calculate higher-order binomial coefficients or the Fibonacci numbers, can be regarded as a one-dimensional cellular automaton in which the value that is assigned to each site of a regular triangular lattice is calculated through the summation of the two numbers above it. In this case, the entities of the automaton are dimensionless integer numbers and the transformation rule is a summation.

Cellular automata were introduced by von Neumann (1) for the simulation of self-reproducing Turing automata and population evolution. In his early contributions, von Neumann denoted the automata as cellular spaces (1). Other authors used

notions like tessellation automata, homogeneous structures, tessellation structures, or iterative arrays. Later applications were mainly in the field of describing non-linear dynamic behavior of fluids and reaction-diffusion systems. During the past decade, cellular automata have increasingly gained momentum for the simulation of microstructure evolution in the materials sciences.

### Formal Description and Classes of Cellular Automata

The local interaction of neighboring lattice sites in a cellular automaton is specified through a set of transformation (switching) rules. Although von Neumann's original automata were designed with deterministic transformation rules, probabilistic transformations are conceivable as well. The value of an arbitrary state variable  $\xi$  assigned to a particular lattice site at a time  $(t_0 + \Delta t)$  is determined by its present state  $(t_0)$  (or its last few states  $t_0, t_0 - \Delta t$ , etc.) and the state of its neighbors (1-4).

Considering the last two time steps for the evolution of a one-dimensional cellular automaton, this can be put formally by writing  $\xi_j^{t_0+\Delta t} = f(\xi_{j-1}^{t_0-\Delta t}, \xi_j^{t_0-\Delta t}, \xi_{j+1}^{t_0-\Delta t}, \xi_{j-1}^{t_0}, \xi_j^{t_0}, \xi_{j+1}^{t_0})$ , where  $\xi_j^{t_0}$  indicates the value of the variable at a time  $t_0$  at the node  $j$ . The positions  $(j+1)$  and  $(j-1)$  indicate the nodes in the immediate neighborhood of position  $j$  (for one dimension). The function  $f$  specifies the set of transformation rules, for instance such as provided by standard discrete finite difference algorithms.

If the state of the node depends only on its nearest neighbors (NN), the array is referred to as von Neumann neighboring (Figure 1a). If both the NN and the next-nearest neighbors (NNN) determine the ensuing state of the node, the array is called

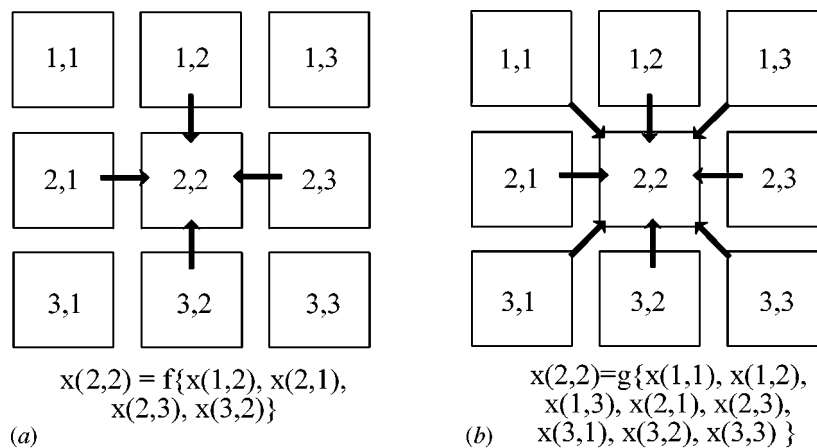


**Figure 1** (a) Example of a two-dimensional von Neumann configuration considering nearest neighbors. (b) Example of a two-dimensional Moore configuration considering both nearest and next-nearest neighbors.

Moore neighboring (Figure 1b) (2). Owing to the discretization of space, the type of neighboring affects the local transformation rates and the evolving morphologies (1–4). For the Moore and other extended configurations, for which a certain medium-range interaction can be introduced among the sites, the transformation rule can in one dimension and for interaction with the last two time steps be rewritten as  $\xi_j^{t_0+\Delta t} = f(\xi_{j-n}^{t_0-\Delta t}, \xi_{j-n+1}^{t_0-\Delta t}, \dots, \xi_{j-1}^{t_0-\Delta t}, \xi_j^{t_0-\Delta t}, \xi_{j+1}^{t_0-\Delta t}, \xi_{j-1}^{t_0}, \xi_j^{t_0}, \xi_{j+1}^{t_0}, \dots, \xi_{j+n-1}^{t_0}, \xi_{j+n}^{t_0})$ , where  $n$  indicates the range of the transformation rule in units of lattice cells.

Even for very simple automata there exists an enormous variety of possible transformation rules. For instance, for a one-dimensional cellular automaton (Boolean, von Neumann neighboring), where each node can have one of two possible ground states, say  $\xi_j = 1$  or  $\xi_j = 0$ , the transformation rule assumes the form  $\xi_j^{t_0+\Delta t} = f(\xi_{j-1}^{t_0}, \xi_j^{t_0}, \xi_{j+1}^{t_0})$ . This simple Boolean configuration defines  $2^8$  possible transformation rules. One of them has the form

if ( $\xi_{j-1}^{t_0} = 1, \xi_j^{t_0} = 1, \xi_{j+1}^{t_0} = 1$ )	then	$\xi_j^{t_0+\Delta t} = 0$	$(1, 1, 1) \rightarrow 0$
if ( $\xi_{j-1}^{t_0} = 1, \xi_j^{t_0} = 1, \xi_{j+1}^{t_0} = 0$ )	then	$\xi_j^{t_0+\Delta t} = 1$	$(1, 1, 0) \rightarrow 1$
if ( $\xi_{j-1}^{t_0} = 1, \xi_j^{t_0} = 0, \xi_{j+1}^{t_0} = 1$ )	then	$\xi_j^{t_0+\Delta t} = 0$	$(1, 0, 1) \rightarrow 0$
if ( $\xi_{j-1}^{t_0} = 1, \xi_j^{t_0} = 0, \xi_{j+1}^{t_0} = 0$ )	then	$\xi_j^{t_0+\Delta t} = 1$	$(1, 0, 0) \rightarrow 1$
if ( $\xi_{j-1}^{t_0} = 0, \xi_j^{t_0} = 1, \xi_{j+1}^{t_0} = 1$ )	then	$\xi_j^{t_0+\Delta t} = 1$	$(0, 1, 1) \rightarrow 1$
if ( $\xi_{j-1}^{t_0} = 0, \xi_j^{t_0} = 1, \xi_{j+1}^{t_0} = 0$ )	then	$\xi_j^{t_0+\Delta t} = 0$	$(0, 1, 0) \rightarrow 0$
if ( $\xi_{j-1}^{t_0} = 0, \xi_j^{t_0} = 0, \xi_{j+1}^{t_0} = 1$ )	then	$\xi_j^{t_0+\Delta t} = 1$	$(0, 0, 1) \rightarrow 1$
if ( $\xi_{j-1}^{t_0} = 0, \xi_j^{t_0} = 0, \xi_{j+1}^{t_0} = 0$ )	then	$\xi_j^{t_0+\Delta t} = 0$	$(0, 0, 0) \rightarrow 0$

This particular transformation rule can be encoded by  $(01011010)_2$ , where the digits in brackets indicate the right-hand side of the table given above, and the  $\xi$  indicates the Boolean description. Its digital description is, of course, only valid for a given arrangement of the corresponding basis. This order is commonly chosen as a decimal row with decreasing value, i.e.,  $(1, 1, 1)$  translates to 111 (one hundred eleven),  $(1, 1, 0)$  to 110 (one hundred ten), and so on. Transforming the binary code into decimal numbers using

$2^7$	$2^6$	$2^5$	$2^4$	$2^3$	$2^2$	$2^1$	$2^0$
0	1	0	1	1	0	1	0

leads to the decimal code number  $90_{10}$ . The digital coding system is commonly used for compactly describing transformation rules for cellular automata in the literature (2–4).

In general terms the number of rules can be calculated by  $k^{(kn)}$ , where  $k$  is the number of states for the cell and  $n$  is the number of neighbors including the core cell. For a two-dimensional automaton with a Moore neighborhood and two possible

cell states (i.e.,  $k=2$  and  $n=9$ )  $2^{29} = 262144$  different transformation rules exist.

If the state of a node is determined by the sum of the neighbor site values, the model is referred to as a totalistic cellular automaton. If the state of a node has a separate dependence on the state itself and on the sum of the values taken by the variables of the neighbors, the model is referred to as an outer totalistic cellular automaton (2–6).

Cellular automata fall into four basic classes of behavior (2–4) (for almost any initial configuration). Class 1 cellular automata evolve after a finite number of time steps to a homogeneous and unique state from which they do not evolve further. Cellular automata in this class exhibit the maximal possible order both at the global and local scale. The geometrical analogy for this class is a limit point in the corresponding phase space. Class 2 cellular automata usually create short period patterns that repeat periodically, typically either recurring after small periods or are stable. Local and global order exhibited is in such automata, although not maximal. Class 2 automata can be interpreted as filters that derive the essence from discrete data sets for a given set of transformation rules. In phase space such systems form a limit cycle. Class 3 cellular automata lead from almost all possible initial states to aperiodic chaotic patterns. The statistical properties of these patterns and the statistical properties of the starting patterns are almost identical at least after a sufficient period of time. The patterns created by class 3 automata are usually self-similar fractal arrays. After sufficiently many time steps, the statistical properties of these patterns are typically the same for almost all initial configurations. Geometrically, class 3 automata form so-called strange attractors in phase space. Class 3 is the most frequent type of cellular automata. With increasing size of the neighborhood and increasing number of possible cell states, the probability to design a class 3 automaton increases for an arbitrary selected rule. Cellular automata in this class can exhibit maximal disorder on both global and local scales. Class 4 cellular automata yield stable, periodic, and propagating structures that can persist over arbitrary lengths of time. Some class 4 automata dissolve after a finite number of steps of time, i.e., the state of all cells becomes zero. In some class 4 automata a small set of stable periodic figures can occur [such as for instance in Conway's "game of life" (5)]. By properly arranging these propagating structures, final states with any cycle length may be obtained. Class 4 automata show a high degree of irreversibility in their time development. They usually reveal more complex behavior and very long transient lengths, having no direct analogue in the field of dynamical systems. The cellular automata in this class can exhibit significant local (not global) order.

These introductory remarks show that the cellular automaton concept is defined in a very general and versatile way. Cellular automata can be regarded as a generalization of discrete calculation methods (1, 2). Their flexibility is due to the fact that, in addition to the use of crisp mathematical expressions as variables and discretized differential equations as transformation rules, automata can incorporate practically any kind of element or rule that is deemed relevant.

## APPLICATION OF CELLULAR AUTOMATA IN MATERIALS SCIENCE

Transforming the abstract rules and properties of general cellular automata into a materials-related simulation concept consists of mapping the values of relevant state variables onto the points of a cellular automaton lattice and using the local finite difference formulations of the partial differential equations of the underlying model as local transformation rules. The particular versatility of the cellular automaton approach for microstructure simulations, particularly in the fields of recrystallization, grain growth, and phase transformation phenomena, is due to its flexibility in considering a large variety of state variables and transformation laws.

The design of such time and space discretized simulations of materials microstructures, which track kinetics and energies in a local fashion, are of interest for two reasons. First, from a fundamental standpoint, it is desirable to understand better the dynamics and the topology of microstructures that arise from the interaction of large numbers of lattice defects, which are characterized by a spectrum of intrinsic properties and interactions in spatially heterogeneous materials. For instance, in the fields of recrystallization and grain growth, the influence of local grain boundary characteristics (mobility, energy), local driving forces, and local crystallographic textures on the final microstructure is of particular interest. Second, from a practical point of view, it is desirable to predict microstructure parameters such as grain size or texture that determine the mechanical and physical properties of real materials subjected to industrial processes from a phenomenological, though sound, physical basis.

Apart from cellular automata, a number of excellent models for discretely simulating recrystallization and grain growth phenomena have been suggested. They can be grouped as multistate kinetic Potts Monte Carlo models, topological boundary dynamics and front-tracking models, and Ginzburg-Landau type phase field kinetic models [see overview in (6)]. However, compared with these approaches, the strength of scaleable kinetic cellular automata is such that they combine the computational simplicity and scalability of a switching model with the physical stringency of a boundary dynamics model. Their objective lies in providing a numerically efficient and at the same time phenomenologically sound method of discretely simulating recrystallization and grain growth phenomena. As far as computational aspects are concerned, cellular automata can be designed to minimize calculation time and reduce code complexity in terms of storage and algorithm. As far as microstructure physics is concerned, they can be designed to provide kinetics, texture, and microstructure on a real space and time scale on the basis of realistic or experimental input data for microtexture, grain boundary characteristics, and local driving forces. The possible incorporation of realistic values, particularly for grain boundary energies and mobilities, deserves particular attention because such experimental data are increasingly available, enabling one to make quantitative predictions.

Cellular automaton simulations are often carried out at an elementary level using atoms, clusters of atoms, dislocation segments, or small crystalline or continuum elements as underlying units. It should be emphasized in particular that those variants that discretize and map microstructure in continuum space are not intrinsically calibrated by a characteristic physical length or timescale. This means that a cellular automaton simulation of continuum systems requires the definition of elementary units and transformation rules that adequately reflect the system behavior at the level addressed. If some of the transformation rules refer to different real timescales (e.g., recrystallization and recovery, bulk diffusion and grain boundary diffusion) it is essential to achieve a correct common scaling of the entire system. The requirement for an adjustment of timescaling among various rules is due to the fact that the transformation behavior of a cellular automaton is sometimes determined by noncoupled Boolean routines rather than by the exact local solutions of coupled differential equations. The same is true when underlying differential equations with entirely different time scales enter the formulation of a set of transformation rules. The scaling problem becomes particularly important in the simulation of nonlinear systems (which applies for most microstructure-based cellular automata). During the simulation, it can be useful to refine or coarsen the scale according to the kinetics (time re-scaling) and spatial resolution (space re-scaling). Because the use of cellular automata is not confined to the microscopic regime, it provides a convenient numerical means for bridging various space and timescales in microstructure simulation.

Important fields where microstructure-based cellular automata have been successfully used in the materials sciences are primary static recrystallization and recovery (6–19), formation of dendritic grain structures in solidification processes (20–26), and related nucleation and coarsening phenomena (27–36). The following is devoted to the simulation of primary static recrystallization. For further study of related microstructural topics, the reader is referred to the references cited above.

## EXAMPLE OF A RECRYSTALLIZATION SIMULATION BY USE OF A PROBABILISTIC CELLULAR AUTOMATON

### Lattice Structure and Transformation Rule

The model for the present recrystallization simulation is designed as a cellular automaton with a probabilistic transformation rule (16–18). Independent variables are time  $t$  and space  $\mathbf{x} = (x_1, x_2, x_3)$ . Space is discretized into an array of equally shaped cells (two- or three-dimensional depending on input data). Each cell is characterized in terms of the dependent variables. These are scalar (mechanical, electromagnetic) and configurational (interfacial) contributions to the driving force and the crystal orientation  $\mathbf{g} = \mathbf{g}(\varphi_1, \phi, \varphi_2)$ , where  $\mathbf{g}$  is the rotation matrix and  $\varphi_1, \phi, \varphi_2$  the Euler angles. The driving force is the negative change in Gibbs enthalpy  $G_t$  per transformed cell. The starting data, i.e., the crystal orientation map and the spatial distribution of the driving force, can be provided by experiment,

i.e., orientation imaging microscopy via electron back scatter diffraction, or by simulation, e.g., a crystal plasticity finite element simulation. Grains or subgrains are mapped as regions of identical crystal orientation, but the driving force may vary inside these areas.

The kinetics of the automaton result from changes in the state of the cells (cell switches). They occur in accord with a switching rule (transformation rule), which determines the individual switching probability of each cell as a function of its previous state and the state of its neighbor cells. The switching rule is designed to map the phenomenology of primary static recrystallization in a physically sound manner. It reflects that the state of a non-recrystallized cell belonging to a deformed grain may change owing to the expansion of a recrystallizing neighbor grain, which grows according to the local driving force and boundary mobility. If such an expanding grain sweeps a non-recrystallized cell, the stored dislocation energy of that cell drops to zero and a new orientation is assigned to it, namely that of the expanding neighbor grain. To put this formally, the switching rule is cast in a probabilistic form of a linearized symmetric rate equation, which describes grain boundary motion in terms of isotropic single-atom diffusion processes perpendicular through a homogeneous planar grain boundary segment under the influence of a decrease in Gibbs energy,

$$\dot{\mathbf{x}} = \mathbf{n} \nu_D \lambda_{\text{gb}} c \left\{ \exp\left(-\frac{\Delta G + \Delta G_t/2}{k_B T}\right) - \exp\left(-\frac{\Delta G - \Delta G_t/2}{k_B T}\right) \right\}, \quad 1.$$

where  $\dot{\mathbf{x}}$  is the grain boundary velocity,  $\nu_D$  the Debye frequency,  $\lambda_{\text{gb}}$  the jump width through the boundary,  $c$  the intrinsic concentration of grain boundary vacancies or shuffle sources,  $\mathbf{n}$  the normal of the grain boundary segment,  $\Delta G$  the Gibbs enthalpy of motion through the interface,  $\Delta G_t$  the Gibbs enthalpy associated with the transformation,  $k_B$  the Boltzmann constant, and  $T$  the absolute temperature. Replacing the jump width by the Burgers vector and the Gibbs enthalpy terms by the total entropy,  $\Delta S$ , and total enthalpy,  $\Delta H$ , leads to a linearized form

$$\dot{\mathbf{x}} \approx \mathbf{n} \nu_D b \exp\left(-\frac{\Delta S}{k_B}\right) \exp\left(-\frac{\Delta H}{k_B T}\right) \left(\frac{pV}{k_B T}\right), \quad 2.$$

where  $p$  is the driving force and  $V$  the atomic volume, which is of the order of  $b^3$  ( $b$  is the magnitude of the Burgers vector). Summarizing these terms reproduces Turnbull's rate expression

$$\dot{\mathbf{x}} = \mathbf{n} m p = \mathbf{n} m_0 \exp\left(-\frac{Q_{\text{gb}}}{k_B T}\right) p, \quad 3.$$

where  $m$  is the mobility. These equations provide a well-known kinetic picture of grain boundary segment motion, where the atomistic processes (including thermal fluctuations, i.e., random thermal backward and forward jumps) are statistically described in terms of the pre-exponential factor of the mobility  $m_0 = m_0(\Delta \mathbf{g}, \mathbf{n})$  and of the activation energy of grain boundary mobility  $Q_{\text{gb}} = Q_{\text{gb}}(\Delta \mathbf{g}, \mathbf{n})$ .

For dealing with competing switches affecting the same cell, the deterministic rate equation can be replaced by a probabilistic analogue that allows one to calculate switching probabilities. For this purpose, Equation 3 is separated into a deterministic part,  $\dot{\mathbf{x}}_0$ , which depends weakly on temperature, and a probabilistic part,  $w$ , which depends strongly on temperature:

$$\begin{aligned}\dot{\mathbf{x}} &= \dot{\mathbf{x}}_0 w = \mathbf{n} \frac{k_B T m_0}{V} \frac{pV}{k_B T} \exp\left(-\frac{Q_{gb}}{k_B T}\right) \quad \text{with} \quad \dot{\mathbf{x}}_0 = \mathbf{n} \frac{k_B T m_0}{V}, \\ w &= \frac{pV}{k_B T} \exp\left(-\frac{Q_{gb}}{k_B T}\right).\end{aligned}\tag{4}$$

The probability factor  $w$  represents the product of the linearized part  $pV/(k_B T)$  and the non-linearized part  $\exp[-Q_{gb}/(k_B T)]$  of the original Boltzmann terms. According to this expression, non-vanishing switching probabilities occur for cells that reveal neighbors with different orientation and a driving force that points in their direction. The automaton considers the first, second (two-dimensional), and third (three-dimensional) neighbor shell for the calculation of the total driving force acting on a cell. The local value of the switching probability depends on the crystallographic character of the boundary segment between such unlike cells.

### Scaling and Normalization

Microstructure-based cellular automata are usually applied to starting data that have a spatial resolution far above the atomic scale. This means that the automaton lattice has a lateral scaling of  $\lambda_m \gg b$ , where  $\lambda_m$  is the scaling length of the cellular automaton lattice and  $b$  the Burgers vector. If a moving boundary segment sweeps a cell, the grain thus grows (or shrinks) by  $\lambda_m^3$  rather than  $b^3$ . Because the net velocity of a boundary segment must be independent of this scaling value of  $\lambda_m$ , an increase in jump width must lead to a corresponding decrease in the grid attack frequency, i.e., to an increase of the characteristic time step and vice versa. For obtaining a scale-independent grain boundary velocity, the grid frequency must be chosen in a way to ensure that the attempted switch of a cell of length  $\lambda_m$  occurs with a frequency much below the atomic attack frequency, which attempts to switch a cell of length  $b$ . This scaling condition, which is prescribed by an external scaling length  $\lambda_m$ , leads to the equation

$$\dot{\mathbf{x}} = \dot{\mathbf{x}}_0 w = \mathbf{n}(\lambda_m \nu) w \quad \text{with} \quad \nu = \frac{k_B T m_0}{V \lambda_m},\tag{5}$$

where  $\nu$  is the eigenfrequency of the chosen lattice characterized by the scaling length  $\lambda_m$ .

The eigenfrequency represents the attack frequency for one particular grain boundary with constant mobility. To use a whole spectrum of mobilities and driving forces in one simulation, it is necessary to normalize the eigenfrequency by a

common grid attack frequency  $\nu_0$ , yielding

$$\dot{\mathbf{x}} = \dot{\mathbf{x}}_0 W = \mathbf{n} \lambda_m \nu_0 \left( \frac{\nu}{\nu_0} \right) W = \hat{\mathbf{x}}_0 \left( \frac{\nu}{\nu_0} \right) W = \hat{\mathbf{x}}_0 \hat{w}. \quad 6.$$

The value of the attack frequency  $\nu_0$ , which is characteristic of the lattice, can be calculated by the assumption that the maximum occurring switching probability cannot be larger than one;

$$\hat{w}^{\max} = \frac{m_0^{\max} p^{\max}}{\lambda_m \nu_0^{\min}} \exp\left(-\frac{Q_{\text{gb}}^{\min}}{k_B T}\right) \leq 1, \quad 7.$$

where  $m_0^{\max}$  is the maximum occurring pre-exponential factor of the mobility,  $p^{\max}$  the maximum possible driving force,  $\nu_0^{\min}$  the minimum allowed grid attack frequency, and  $Q_{\text{gb}}^{\min}$  the minimum occurring activation energy. With  $\hat{w}^{\max} = 1$ , one obtains the normalization frequency as a function of the upper bound input data.

$$\nu_0^{\min} = \frac{m_0^{\max} p^{\max}}{\lambda_m} \exp\left(-\frac{Q_{\text{gb}}^{\min}}{k_B T}\right). \quad 8.$$

This frequency and the local values of the mobility and the driving force lead to

$$\begin{aligned} \hat{w}^{\text{local}} &= \frac{m_0^{\text{local}} p^{\text{local}}}{\lambda_m \nu_0^{\min}} \exp\left(-\frac{Q_{\text{gb}}^{\text{local}}}{k_B T}\right) \\ &= \left(\frac{m_0^{\text{local}}}{m_0^{\max}}\right) \left(\frac{p^{\text{local}}}{p^{\max}}\right) \exp\left(-\frac{(Q_{\text{gb}}^{\text{local}} - Q_{\text{gb}}^{\min})}{k_B T}\right) = \left(\frac{m^{\text{local}} p^{\text{local}}}{m^{\max} p^{\max}}\right). \end{aligned} \quad 9.$$

This expression is the central switching equation of the algorithm. One can interpret this equation also in terms of the local time  $t = \lambda_m / \dot{\mathbf{x}}$ , which is required by a grain boundary with velocity  $\dot{\mathbf{x}}$  to sweep an automaton cell of size  $\lambda_m$ .

$$\hat{w}^{\text{local}} = \left(\frac{m^{\text{local}} p^{\text{local}}}{m^{\max} p^{\max}}\right) = \left(\frac{\dot{\mathbf{x}}^{\text{local}}}{\dot{\mathbf{x}}^{\max}}\right) = \left(\frac{t^{\max}}{t^{\text{local}}}\right). \quad 10.$$

Equation 9 shows that the local switching probability can be quantified by the ratio of the local and the maximum mobility  $m^{\text{local}}/m^{\max}$ , which is a function of the grain boundary character and by the ratio of the local and the maximum driving pressure  $p^{\text{local}}/p^{\max}$ . The probability of the fastest occurring boundary segment (characterized by  $m_0^{\text{local}} = m_0^{\max}$ ,  $p^{\text{local}} = p^{\max}$ ,  $Q_{\text{gb}}^{\text{local}} = Q_{\text{gb}}^{\min}$ ) to realize a cell switch is equal to 1.

Equation 9 shows that an increasing cell size does not influence the switching probability but only the time step elapsing during an attempted switch. This relationship is obvious since the volume to be swept becomes larger, which requires more time. The characteristic time constant of the simulation  $\Delta t$  is  $1/\nu_0^{\min}$ .

Although Equation 9 allows one to calculate the switching probability of a cell as a function of its previous state and the state of the neighbor cells, the actual decision about a cell switch is made by a Monte Carlo step. The use of random numbers ensures that all cell switches are sampled according to their proper statistical weight, i.e., according to the local driving force and mobility between cells. The simulation proceeds by calculating the individual local switching probabilities  $\hat{w}^{\text{local}}$  for each cell and evaluating them using a Monte Carlo algorithm. This means that for each cell the calculated switching probability is compared with a randomly generated number  $r$ , which lies between 0 and 1. The switch is accepted if the random number is equal or smaller than the calculated switching probability. Otherwise the switch is rejected.

$$\text{Random number } r \text{ between 0 and 1} \left\{ \begin{array}{l} \text{accept switch if } r \leq \left( \frac{m^{\text{local}} p^{\text{local}}}{m^{\text{max}} p^{\text{max}}} \right) \\ \text{reject switch if } r > \left( \frac{m^{\text{local}} p^{\text{local}}}{m^{\text{max}} p^{\text{max}}} \right) \end{array} \right. \quad 11.$$

Except for the probabilistic evaluation of the analytically calculated transformation probabilities, the approach is entirely deterministic. Thermal fluctuations other than already included via Turnbull's rate equation are not permitted. The use of realistic or even experimental input data for the grain boundaries enables one to make predictions on a real time and space scale. The switching rule is scalable to any mesh size and to any spectrum of boundary mobility and driving force data. The state update of all cells is made in synchrony.

### Simulation of Primary Static Recrystallization and Comparison to Avrami-Type Kinetics

Figure 2 shows the kinetics and three-dimensional microstructures of a recrystallizing aluminum single crystal. The initial deformed crystal had a uniform Goss orientation (011)[100] and a dislocation density of  $10^{15} \text{ m}^{-2}$ . The driving force was from the stored elastic energy provided by the dislocations. In order to compare the predictions with analytical Avrami kinetics, recovery and driving forces arising from local boundary curvature were not considered. The simulation used site saturated nucleation conditions, i.e., the nuclei at  $t=0$  s were statistically distributed in physical space and orientation space. The grid size was  $10 \times 10 \times 10 \mu\text{m}^3$ . The cell size was  $0.1 \mu\text{m}$ . All grain boundaries had the same mobility using an activation energy of the grain boundary mobility of 1.3 eV and a pre-exponential factor of the boundary mobility of  $m_0 = 6.2 \cdot 10^{-6} \text{ m}^3/(\text{N}\cdot\text{s})$  (37). Small angle grain boundaries had a mobility of zero. The temperature was 800 K. The time constant of the simulation was 0.35 s.

Figure 3 shows the kinetics for a number of three-dimensional recrystallization simulations with site-saturated nucleation conditions and identical mobility for all grain boundaries. The different curves correspond to different initial numbers

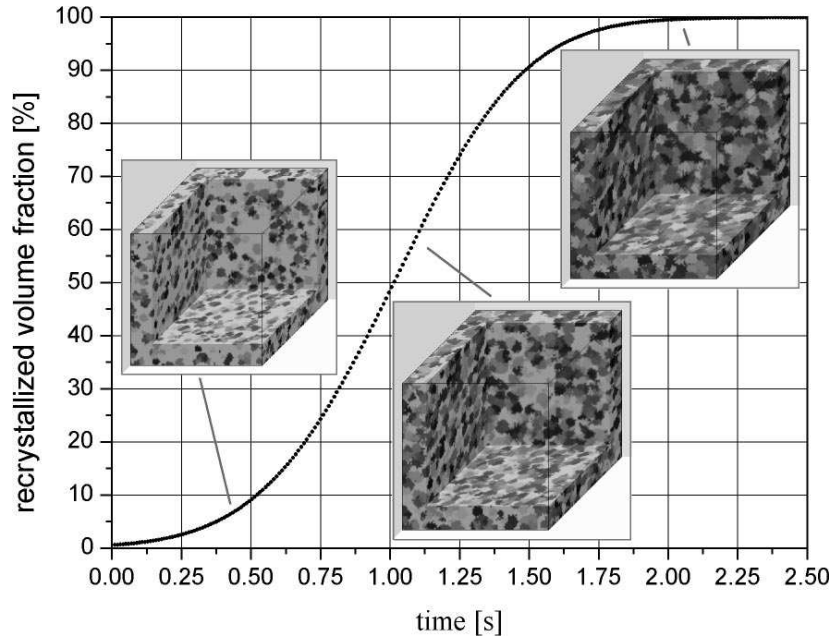


**Figure 2** Kinetics and microstructure of recrystallization in a plastically strained aluminum single crystal. The deformed crystal had a uniform (011)[100] orientation and a uniform dislocation density of  $10^{15} \text{ m}^{-2}$ . Simulation parameter: site-saturated nucleation; lattice size,  $10 \times 10 \times 10 \mu\text{m}^3$ ; cell size,  $0.1 \mu\text{m}$ ; activation energy of large-angle grain boundary mobility, 1.3 eV; pre-exponential factor of large-angle boundary mobility,  $m_0 = 6.2 \cdot 10^{-6} \text{ m}^3/(\text{N} \cdot \text{s})$ ; temperature, 800 K; time constant 0.35 s.

of nuclei. The initial number of nuclei varied between 9624 (pseudo-nucleation energy of 3.2 eV) and 165 (pseudo-nucleation energy of 6.0 eV). The curves (Figure 3a) all show a typical Avrami shape, and the logarithmic plots (Figure 3b) reveal Avrami exponents between 2.86 and 3.13, which is in good accord with the analytical value of 3.0 for site-saturated conditions. The simulations with a very high initial density of nuclei reveal a more pronounced deviation of the Avrami exponent with values around 2.7 during the beginning of recrystallization. This deviation from the analytical behavior is due to lattice effects: While the analytical derivation assumes a vanishing volume for newly formed nuclei, the cellular automaton has to assign one lattice point to each new nucleus.

Figure 4 shows the effect of grain boundary mobility on growth selection. Whereas in Figure 4a all boundaries have the same mobility, in Figure 4b one grain boundary has a larger mobility than the others (activation energy of the mobility of 1.35 eV instead of 1.40 eV) and consequently grew much faster than the neighboring grains that finally ceased to grow. The grains in this simulation all grew into a heavily deformed single crystal.

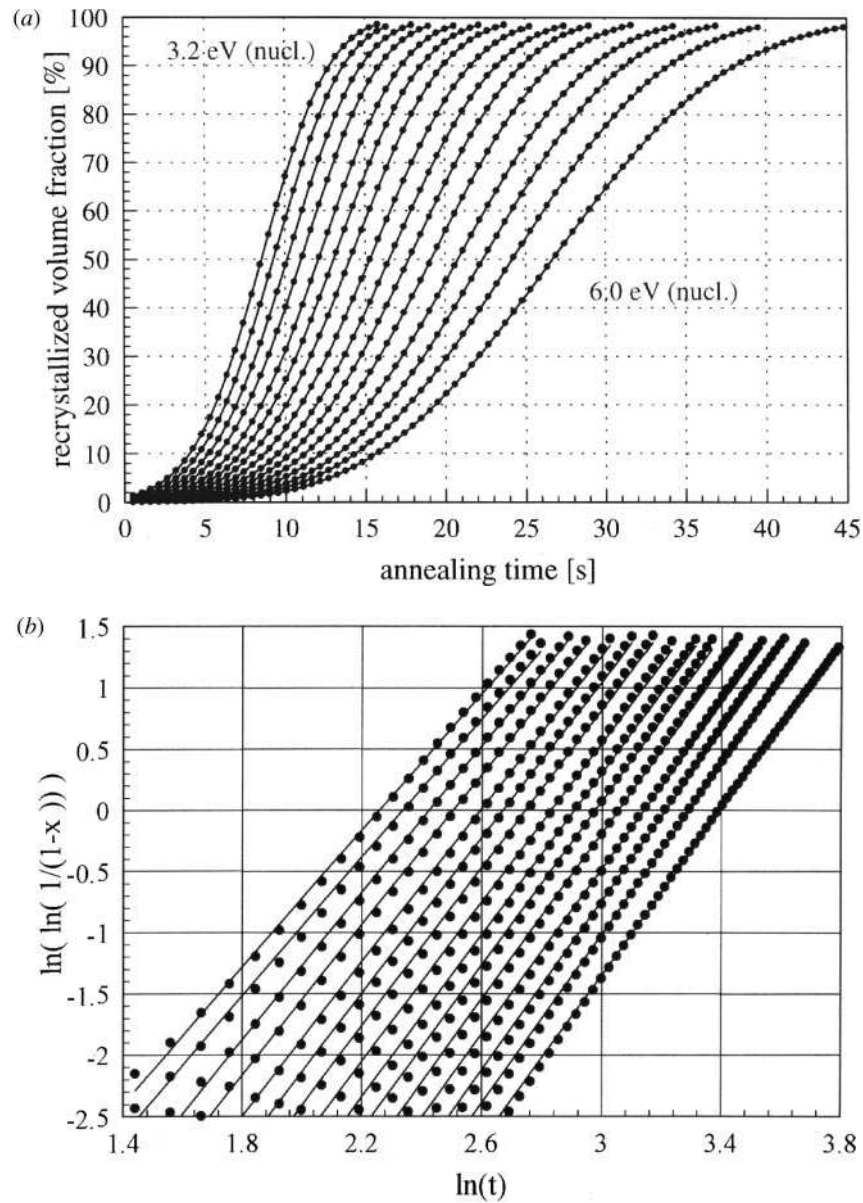


**Figure 3** Kinetics for various three-dimensional recrystallization simulations with site-saturated nucleation conditions and identical mobility for all grain boundaries. The different curves correspond to different initial numbers of nuclei. The initial number of nuclei varied between 9624 (pseudo-nucleation energy of 3.2 eV) and 165 (pseudo-nucleation energy of 6.0 eV). (a) Avrami diagrams, (b) logarithmic diagrams showing Avrami exponents between 2.86 and 3.13.

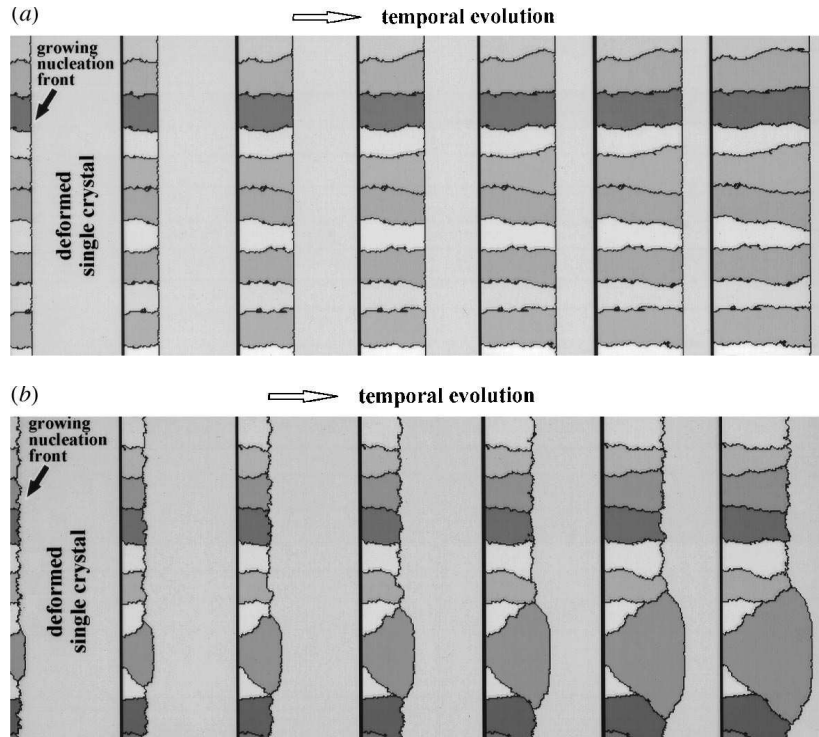


**Figure 4** Effect of grain boundary mobility on growth selection. All grains grow into a deformed single crystal. (a) All grain boundaries have the same mobility. (b) One grain boundary has a larger mobility than the others (activation energy of the mobility of 1.35 eV instead of 1.40 eV) and grows faster than the neighboring grains.

### Examples of Coupling Cellular Automata with Crystal Plasticity Finite Element Models for Predicting Recrystallization

Simulation approaches such as the crystal plasticity finite element method or cellular automata are increasingly gaining momentum as tools for spatial and temporal discrete prediction methods for microstructures and textures. The major advantage of such approaches is that they consider material heterogeneity as opposed to classical statistical approaches, which are based on the assumption of material homogeneity.

Although the average behavior of materials during deformation and heat treatment can sometimes be sufficiently well described without considering local effects, prominent examples exist where substantial progress in understanding and tailoring material response can only be attained by taking material heterogeneity into account. For instance, in the field of plasticity, the quantitative investigation of ridging and roping or related surface defects observed in sheet metals requires

knowledge about local effects such as the grain topology or the form and location of second phases. In the field of heat treatment, the origin of the Goss texture in transformer steels, the incipient stages of cube texture formation during primary recrystallization of aluminum, the reduction of the grain size in microalloyed low carbon steel sheets, and the development of strong  $\{111\}\langle uvw \rangle$  textures in steels can hardly be predicted without incorporating local effects such as the orientation and location of recrystallization nuclei and the character and properties of the grain boundaries surrounding them.

Although spatially discrete microstructure simulations have already profoundly enhanced our understanding of microstructure and texture evolution over the past decade, their potential is sometimes simply limited by an insufficient knowledge about the external boundary conditions that characterize the process and an insufficient knowledge about the internal starting conditions, which are, to a large extent, inherited from the preceding process steps. It is thus an important goal to improve the incorporation of both types of information into such simulations. External boundary conditions prescribed by real industrial processes are often spatially non-homogeneous. They can be investigated using experiments or process simulations that consider spatial resolution. Spatial heterogeneities in the internal starting conditions, i.e., in the microstructure and texture, can be obtained from experiments or microstructure simulations that include spatial resolution.

### Coupling, Scaling, and Boundary Conditions

In the present example, the results obtained from a crystal plasticity finite element simulation were used to map a starting microstructure for a subsequent discrete recrystallization simulation carried out with a probabilistic cellular automaton. The finite element model was used to simulate a plane strain compression test conducted on aluminum with columnar grain structure to a total logarithmic strain of  $\varepsilon = -0.434$ . Details about the finite element model are given elsewhere (17, 18, 38, 39). The values of the state variables (dislocation density, crystal orientation) given at the integration points of the finite element mesh were mapped on the regular lattice of a two-dimensional cellular automaton. Whereas the original finite element mesh consisted of 36977 quadrilateral elements, the cellular automaton lattice consisted of 217600 discrete points. The values of the state variables at each of the integration points were assigned to the new cellular automaton lattice points, which fell within the Wigner-Seitz cell corresponding to that integration point. The Wigner-Seitz cells of the finite element mesh were constructed from cell walls that were the perpendicular and bisected planes of all lines connecting neighboring integration points, i.e., the integration points were in the centers of the Wigner-Seitz cells.

In the present example, the original size of the specimen providing the input microstructure to the crystal plasticity finite element simulations gave a lattice point spacing of  $\lambda_m = 61.9 \mu\text{m}$ . The maximum driving force in the region arising from the stored dislocation density amounted to about 1 MPa. The temperature dependence of the shear modulus and of the Burgers vector was considered in the calculation of the driving force. The grain boundary mobility in the region was characterized by an activation energy of the grain boundary mobility of 1.46 eV and a

pre-exponential factor of the grain boundary mobility of  $m_0 = 8.3 \times 10^{-3} \text{ m}^3/(\text{N s})$ . Together with the scaling length  $\lambda_m = 61.9 \text{ }\mu\text{m}$ , these data were used for the calculation of the timestep  $\Delta t = 1/v_0^{\text{min}}$  and of the local switching probabilities  $\hat{w}^{\text{local}}$ . The annealing temperature was 800 K. Large-angle grain boundaries were characterized by an activation energy for the mobility of 1.3 eV. Small-angle grain boundaries were assumed to be immobile.

### Nucleation Criterion

The nucleation process during primary static recrystallization has been explained for pure aluminum in terms of discontinuous subgrain growth (40). According to this model, nucleation takes place in areas that reveal high misorientations among neighboring subgrains and a high local driving force for curvature driven discontinuous subgrain coarsening. The present simulation approach works above the subgrain scale, i.e., it does not explicitly describe cell walls and subgrain coarsening phenomena. Instead, it incorporates nucleation on a more phenomenological basis using the kinetic and thermodynamic instability criteria known from classical recrystallization theory (see, e.g., 40).

The kinetic instability criterion means that a successful nucleation process leads to the formation of a mobile large-angle grain boundary that can sweep the surrounding deformed matrix. The thermodynamic instability criterion means that the stored energy changes across the newly formed large-angle grain boundary providing a net driving force that pushes it forward into the deformed matter. Nucleation in this simulation is performed in accord with these two aspects: Potential nucleation sites must fulfill both the kinetic and the thermodynamic instability criteria.

This nucleation model does not create any new orientations: At the beginning of the simulation, the thermodynamic criterion (the local value of the dislocation density) was first checked for all lattice points. If the dislocation density was larger than some critical value of its maximum value in the sample, the cell was spontaneously recrystallized without any orientation change, i.e., a dislocation density of zero was assigned to it, and the original crystal orientation was preserved. In the next step, the ordinary growth algorithm was employed according to Equations 1–11, i.e., the kinetic conditions for nucleation were checked by calculating the misorientations among all spontaneously recrystallized cells (preserving their original crystal orientation) and their immediate neighborhood considering the first, second, and third neighbor shell. If any such pair of cells revealed a misorientation above  $15^\circ$ , the cell flip of the unrecrystallized cell was calculated according to its actual transformation probability, Equation 9. In case of a successful cell flip, the orientation of the first recrystallized neighbor cell was assigned to the flipped cell.

### Predictions and Interpretation

Figures 5–7 show simulated microstructures for site-saturated spontaneous nucleation in all cells with a dislocation density larger than 50% of the maximum value (in Figure 5), larger than 60% of the maximum value (in Figure 6),

and larger than 70% of the maximum value (in Figure 7). Each figure shows a set of four subsequent microstructures during recrystallization.

The upper graphs in Figures 5–7 show the evolution of the stored dislocation densities. The gray areas are recrystallized, i.e., the stored dislocation content of the affected cells was dropped to zero. The lower graphs represent the microtexture images where each color represents a specific crystal orientation. The color level is determined as the magnitude of the Rodriguez orientation vector using the cube component as reference. The fat white lines in both types of figures indicate grain boundaries with misorientations above  $15^\circ$  irrespective of the rotation axis. The thin green lines indicate misorientations between  $5^\circ$  and  $15^\circ$  irrespective of the rotation axis.

The incipient stages of recrystallization in Figure 5 (cells with 50% of the maximum occurring dislocation density undergoing spontaneous nucleation without orientation change) reveal that nucleation is concentrated in areas with large accumulated local dislocation densities. As a consequence, the nuclei form clusters of similarly oriented new grains (e.g., Figure 5a). Less deformed areas between the bands reveal a very small density of nuclei. Logically, the subsequent stages of recrystallization (Figure 5b–d) reveal that the nuclei do not sweep the surrounding deformation structure freely as described by Avrami-Johnson-Mehl theory but impinge upon each other and thus compete at an early stage of recrystallization.

Figure 6 (using 60% of the maximum occurring dislocation density as threshold for spontaneous nucleation) also reveals strong nucleation clusters in areas with high dislocation densities. Owing to the higher threshold value for a spontaneous cell flip, nucleation outside of the deformation bands occurs very rarely. Similar observations hold for Figure 7 (70% threshold value). It also shows an increasing grain size as a consequence of the reduced nucleation density.

The deviation from Avrami-Johnson-Mehl type growth, i.e., the early impingement of neighboring crystals, is also reflected by the overall kinetics that differ from the classical sigmoidal curve that is found for homogeneous nucleation conditions. Figure 8 shows the kinetics of recrystallization (for the simulations with different threshold dislocation densities for spontaneous nucleation) (Figures 5–7). All curves reveal a flattened shape compared with the analytical model. The high offset value for the curve with 50% critical dislocation density is due to the small threshold value for a spontaneous initial cell flip. This means that 10% of all cells undergo initial site saturated nucleation. Figure 9 shows the corresponding Cahn-Hagel diagrams. It is found that the curves increasingly flatten and drop with an increasing threshold dislocation density for spontaneous recrystallization.

Interestingly, in all three simulation series where spontaneous nucleation took place in areas with large local dislocation densities, the kinetic instability criterion was usually also well enough fulfilled to enable further growth of these freshly recrystallized cells. In this context, it is notable that both instability criteria were treated entirely independently in this simulation. In other words, only those spontaneously recrystallized cells that subsequently found a misorientation above  $15^\circ$  to at least one non-recrystallized neighbor cell were able to expand further.

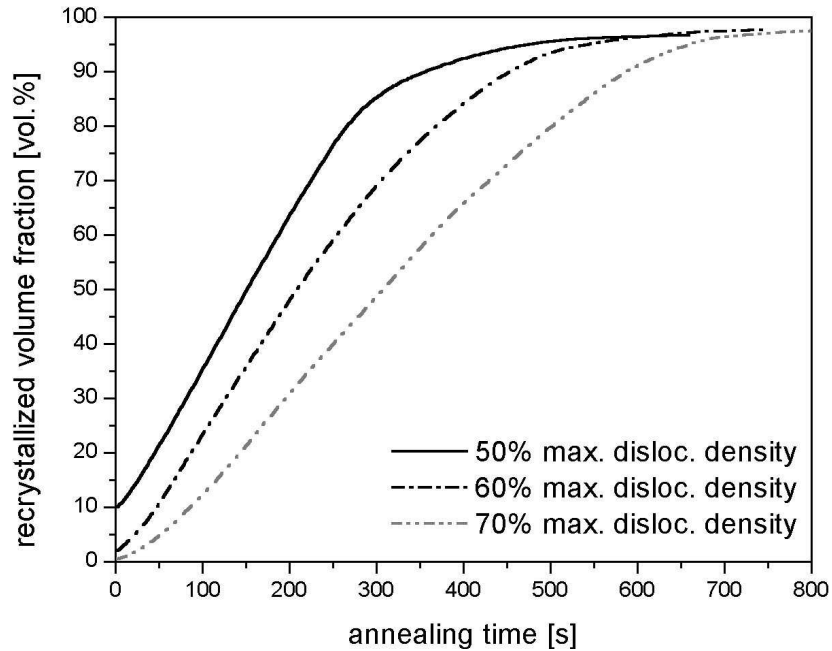


**Figure 8** Kinetics of the recrystallization simulations shown in Figures 5–7. Annealing temperature, 800 K; scaling length  $\lambda_m = 61.9 \mu\text{m}$ .

This makes the essential difference between a potential nucleus and a successful nucleus. Translating this observation into the initial deformation microstructure means that in the present example high dislocation densities and large local lattice curvatures typically occur in close neighborhood or even at the same sites.

Another essential observation is that the nucleation clusters are particularly concentrated in macroscopical deformation bands formed as diagonal instabilities through the sample thickness. Generic intrinsic nucleation inside heavily deformed grains, however, occurs rarely. Only the simulation with a very small threshold value of 50% of the maximum dislocation density as a precondition for a spontaneous energy drop shows some successful nucleation events outside the large bands. But even then, nucleation is successful only at former grain boundaries where orientation changes occur naturally. Summarizing this argument means that there might be a transition from extrinsic nucleation such as inside bands or related large-scale instabilities to intrinsic nucleation inside grains or close to existing grain boundaries. It is likely that both types of nucleation deserve separate attention. As far as the strong nucleation in macroscopic bands is concerned, future consideration should be placed on issues such as the influence of external friction conditions and sample geometry on nucleation. Both aspects strongly influence through thickness shear localization effects.

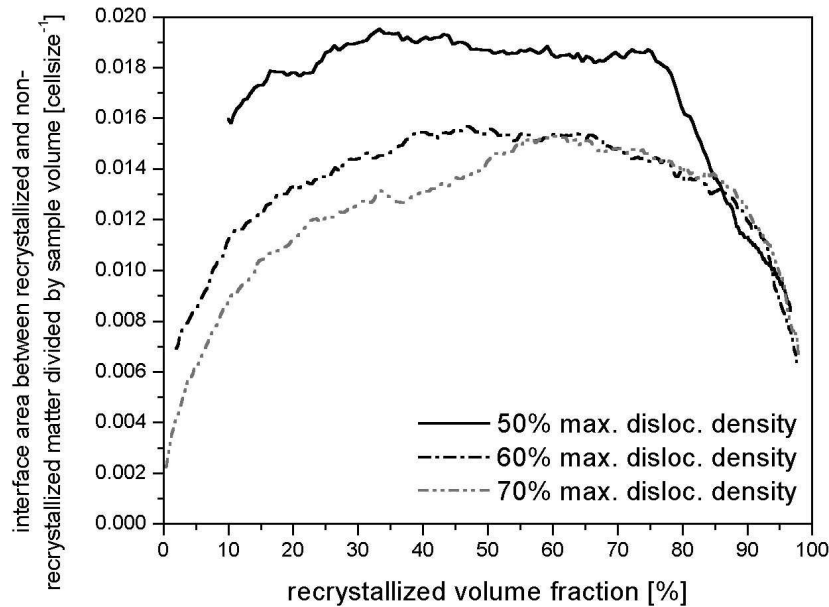


**Figure 9** Simulated interface fractions between recrystallized and non-recrystallized material for the recrystallization simulations shown in Figures 5–7. Annealing temperature, 800 K; scaling length  $\lambda_m = 61.9 \mu\text{m}$ .

Another result of relevance is the partial recovery of deformed material. Figures 5*d*, 6*d*, and 7*d* reveal small areas where moving large-angle grain boundaries did not entirely sweep the deformed material. An analysis of the state variable values at these coordinates and of the grain boundaries involved substantiates that insufficient misorientations, not insufficient driving forces, between the deformed and the recrystallized areas—entailing a drop in grain boundary mobility—were responsible for this effect. This mechanism is referred to as orientation pinning.

### Simulation of Nucleation Topology Within a Single Grain

Recent efforts in simulating recrystallization phenomena on the basis of crystal plasticity finite element or electron microscopy input data are increasingly devoted to tackling the question of nucleation. Here it must be stated clearly that mesoscale cellular automata can neither directly map the physics of a nucleation event nor develop any novel theory for nucleation at the subgrain level. However, cellular automata can predict the topological evolution and competition among growing nuclei during the incipient stages of recrystallization. The initial nucleation criterion itself must be incorporated in a phenomenological form.

This section deals with such an approach for investigating nucleation topology. The simulation was again started using a crystal plasticity finite element

approach. The crystal plasticity model set-up consisted in a single aluminum grain with face centered cubic crystal structure and 12  $\{111\}\langle 1\bar{1}0\rangle$  slip systems embedded in a plastic continuum, which had the elastic-plastic properties of an aluminum polycrystal with random texture. The crystallographic orientation of the aluminum grain in the center was  $\varphi_1 = 32^\circ$ ,  $\phi = 85^\circ$ ,  $\varphi_2 = 85^\circ$ . The entire aggregate was plane strain deformed to 50% thickness reduction (given as  $\Delta d/d_0$ , where  $d$  is the actual sample thickness and  $d_0$  its initial thickness). The resulting data (dislocation density, orientation distribution) were then used as input data for the ensuing cellular automaton recrystallization simulation. The distribution of the dislocation density taken from all integration points of the finite element simulation is given in Figure 10.

Nucleation was initiated as outlined in detail above, i.e., each lattice point that had a dislocation density above some critical value ( $500 \times 10^{13} \text{ m}^{-2}$  in the present

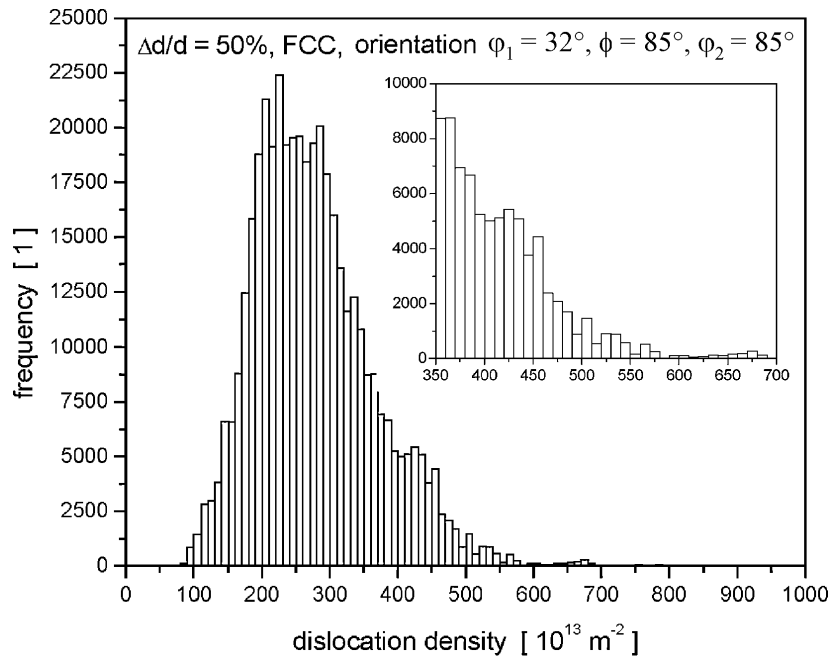


**Figure 10** Distribution of the simulated dislocation density in a deformed aluminum grain embedded in a plastic aluminum continuum. The simulation was performed by using a crystal plasticity finite element approach. The set-up consisted of a single aluminum grain (orientation:  $\varphi_1 = 32^\circ$ ,  $\phi = 85^\circ$ ,  $\varphi_2 = 85^\circ$  in Euler angles), with face centered cubic crystal structure and 12  $\{111\}\langle 1\bar{1}0\rangle$  slip systems, that was embedded in a plastic continuum, which had the elastic-plastic properties of an aluminum polycrystal with random texture. The sample was plane strain deformed to 50% thickness reduction. The resulting data (dislocation density, orientation distribution) were used as input data for a cellular automaton recrystallization simulation.

case; see Figure 10) of the maximum value in the sample was spontaneously recrystallized without orientation change. In the ensuing step, the growth algorithm was started according to Equations 1–11, i.e., a nucleus could only expand further if it was surrounded by lattice points of sufficient misorientation (above  $15^\circ$ ). In order to concentrate on recrystallization in the center grain, the nuclei could not expand into the surrounding continuum material.

Figures 11*a–c* show the change in dislocation density during recrystallization (Figure 11*a*: 9% of the entire sample recrystallized, 32.1 s; Figure 11*b*: 19% of the entire sample recrystallized, 45.0 s; Figure 11*c*: 29.4% of the entire sample recrystallized, 56.3 s). The color scale marks the dislocation density of each lattice point in units of  $10^{13} \text{ m}^{-2}$ . The white areas are recrystallized. The surrounding blue area indicates the continuum material in which the grain is embedded (and into which recrystallization was not allowed to proceed). Figures 12*a–c* show the topology of the evolving nuclei without coloring the as-deformed volume. All recrystallized grains are colored to indicate their crystal orientation. The non-recrystallized material and the continuum surrounding the grain are colored white.

Figure 13 shows the volume fractions of the growing nuclei during recrystallization as a function of annealing time (800 K). The data reveal that two groups of nuclei occur: The first class of nuclei shows some growth in the beginning but no further expansion during the later stages of the anneal. The second class of nuclei

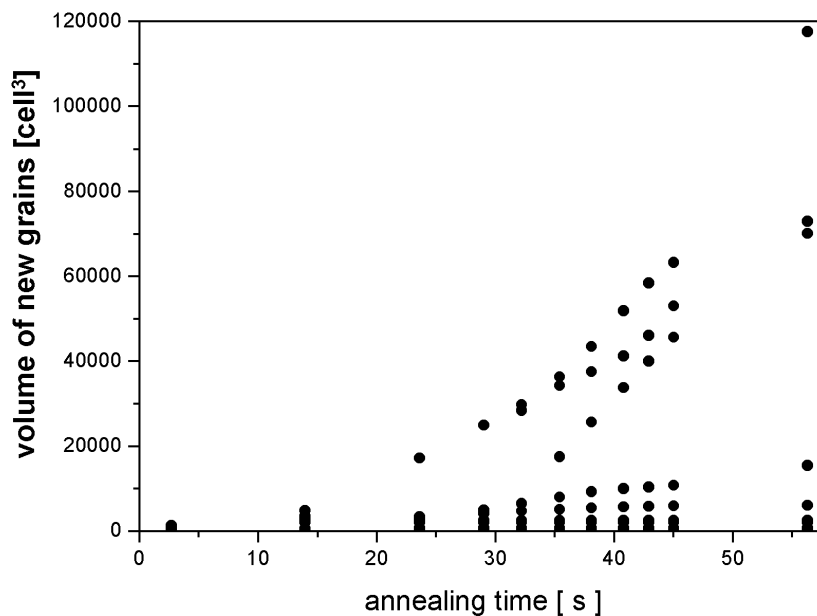


**Figure 13** Volume fractions of the growing nuclei in Figure 11 during recrystallization as a function of annealing time (800 K).

shows strong and steady growth during the entire recrystallization time. The first group could be considered non-relevant nuclei, the second group could be termed relevant nuclei. The spread in the evolution of nucleation topology after their initial formation can be attributed to nucleation clustering, orientation pinning, growth selection, or driving force selection phenomena. Nucleation clustering means that areas with localization of strain and misorientation produce high local nucleation rates. This entails clusters of newly formed nuclei where competing crystals impinge on each other at an early stage of recrystallization so that only some of the newly formed grains of each cluster can expand further, which is another example of orientation pinning, as described above. In other words, some nuclei expand during growth into areas where the local misorientation drops below  $15^\circ$ . Growth selection is a phenomenon where some grains grow significantly faster than others due to a local advantage originating from higher grain boundary mobility such as shown in Figure 4*b*. Typical examples are the  $40^\circ$   $\langle 111 \rangle$  rotation relationship in aluminum or the  $27^\circ$   $\langle 110 \rangle$  rotation relationship in iron-silicon, both of which are known to have a growth advantage [e.g., (40)]. Driving force selection is a phenomenon where some grains grow significantly faster than others due to a local advantage in driving force (shear bands, microbands, heavily deformed grain).

## CONCLUSIONS AND OUTLOOK

We have reviewed the fundamentals and some applications of cellular automata in the field of microstructure research, with special attention given to the fundamentals of mapping rate formulations for interfaces and driving forces on cellular grids. Some applications were discussed from the field of recrystallization theory.

The future of the cellular automaton method in the field of mesoscale materials science lies most likely in the discrete simulation of equilibrium and non-equilibrium phase transformation phenomena. The particular advantage of automata in this context is their versatility with respect to the constitutive ingredients, to the consideration of local effects, and to the modification of the grid structure and the interaction rules. In the field of phase transformation simulations, the constitutive ingredients are the thermodynamic input data and the kinetic coefficients. Both sets of input data are increasingly available from theory and experiment, rendering cellular automaton simulations more and more realistic. The second advantage, i.e., the incorporation of local effects will improve our understanding of cluster effects, such as those arising from the spatial competition of expanding neighboring spheres already in the incipient stages of transformations. The third advantage, i.e., the flexibility of automata with respect to the grid structure and the interaction rules, is probably the most important aspect for novel future applications. By introducing more global interaction rules (in addition to the local rules) and long-range or even statistical elements, in addition to the local rules for the state update, cellular automata could be established as a means for solving some of the intricate scale problems that are often encountered in the materials sciences. It is conceivable that for certain mesoscale problems, such as

the simulation of transformation phenomena in heterogeneous materials in dimensions far beyond the grain scale, cellular automata can occupy a role between the discrete atomistic approaches and statistical Avrami-type approaches.

The major drawback of the cellular automaton method in the field of transformation simulations is the absence of solid approaches for the treatment of nucleation phenomena. Although basic assumptions about nucleation sites, rates, and textures can often be included on an empirical basis as a function of the local values of the state variables, intrinsic physically based phenomenological concepts such as those found, to a certain extent, in the Ginzburg-Landau framework (in case of the spinodal mechanism) are not available for automata. Hence, it might be advantageous in future work to combine Ginzburg-Landau-type phase field approaches with the cellular automaton method. For instance the (spinodal) nucleation phase could then be treated with a phase field method and the resulting microstructure could be further treated with a cellular automaton simulation.

**The Annual Review of Materials Research is online at  
<http://matsci.annualreviews.org>**

#### LITERATURE CITED

1. von Neumann J. 1963. In *Papers of John von Neumann on Computing and Computer Theory*, Vol. 12. Charles Babbage Inst. Reprint Ser. History of Computing, ed. W Aspray, A Burks. Cambridge, MA: MIT Press
2. Wolfram S, ed. 1986. *Theory and Applications of Cellular Automata, Advanced Series on Complex Systems, Selected Papers 1983-1986*, Vol. 1. Singapore: World Sci
3. Wolfram S. 1983. *Rev. Mod. Phys.* 55:601-22
4. Minsky M. 1967. *Computation: Finite and Infinite Machines*. Englewood Cliffs, NJ: Prentice-Hall
5. Conway JH. 1971. *Regular Algebra and Finite Machines*. London: Chapman & Hall
6. Raabe D. 1998. *Computational Materials Science*. Weinheim: Wiley
7. Hesselbarth HW, Göbel IR. 1991. *Acta Metall.* 39:2135-44
8. Pezzee CE, Dunand DC. 1994. *Acta Metall.* 42:1509-22
9. Sheldon RK, Dunand DC. 1996. *Acta Mater.* 44:4571-82
10. Davies CHJ. 1995. *Scripta Metall. Mater.* 33:1139-54
11. Marx V, Raabe D, Gottstein G. 1995. *Proc. 16th RISØ Int. Symp. Mater. Sci. Materials: Microstructural and Crystallographic Aspects of Recrystallization*, ed. N Hansen, D Juul Jensen, YL Liu, B Ralph, pp. 461-66. Roskilde, Denmark: RISO Natl. Lab
12. Marx V, Raabe D, Engler O, Gottstein G. 1997. *Textures Microstruct.* 28:211-18
13. Marx V, Reher FR, Gottstein G. 1998. *Acta Mater.* 47:1219-30
14. Davies CHJ. 1997. *Scripta Mater.* 36:35-46
15. Davies CHJ, Hong L. 1999. *Scripta Mater.* 40:1145-52
16. Raabe D. 1999. *Philos. Mag. A* 79:2339-58
17. Raabe D, Becker R. 2000. *Modelling Simulation Mater. Sci. Eng.* 8:445-62
18. Raabe D. 2000. *Comput. Mater. Sci.* 19:13-26
19. Raabe D, Roters F, Marx V. 1996. *Textures Microstruct.* 26-27:611-35
20. Cortie MB. 1993. *Metall. Trans. B* 24: 1045-52

21. Brown SGR, Williams T, Spittle JA. 1994. *Acta Metall.* 42:2893–906
22. Gandin CA, Rappaz M. 1997. *Acta Metall.* 45:2187–98
23. Gandin CA. 2001. *Adv. Eng. Mater.* 3:303–6
24. Gandin CA, Desbiolles JL, Thevoz PA. 1999. *Metall. Mater. Trans. A* 30:3153–72
25. Spittle JA, Brown SGR. 1995. *J. Mater. Sci.* 30:3989–402
26. Brown SGR, Clarke GP, Brooks AJ. 1995. *Mater. Sci. Technol.* 11:370–82
27. Spittle JA, Brown SGR. 1994. *Acta Metall.* 42:1811–20
28. Kumar M, Sasikumar R, Nair P, Kesavan R. 1998. *Acta Mater.* 46:6291–304
29. Brown SGR. 1998. *J. Mater. Sci.* 33:4769–82
30. Yanagita T. 1999. *Phys. Rev. Lett.* 1999: 3488–92
31. Koltsova EM, Nenaglyadkin IS, Kolosov AY, Dovi VA. 2000. *Russ. J. Phys. Chem.* 74:85–91
32. Geiger J, Roos A, Barkoczy P. 2001. *Acta Mater.* 49:623–29
33. Liu Y, Baudin T, Penelle R. 1996. *Scripta Mater.* 34:1679–86
34. Karapiperis T. 1995. *J. Stat. Phys.* 81:165–74
35. Young MJ, Davies CHJ. 1999. *Scripta Mater.* 41:697–708
36. Kortluke O. 1998. *J. Phys. A* 31:9185–98
37. Gottstein G, Shvindlerman LS. 1999. *Grain Boundary Migration in Metals—Thermodynamics, Kinetics, Applications.* Boca Raton, FL: CRC
38. Becker RC. 1991. *Acta Metall. Mater.* 39: 1211–30
39. Becker RC, Panchanadeeswaran S. 1995. *Acta Metall. Mater.* 43:2701–19
40. Humphreys FJ, Hatherly M. 1995. *Recrystallization and Related Annealing Phenomena.* New York: Pergamon

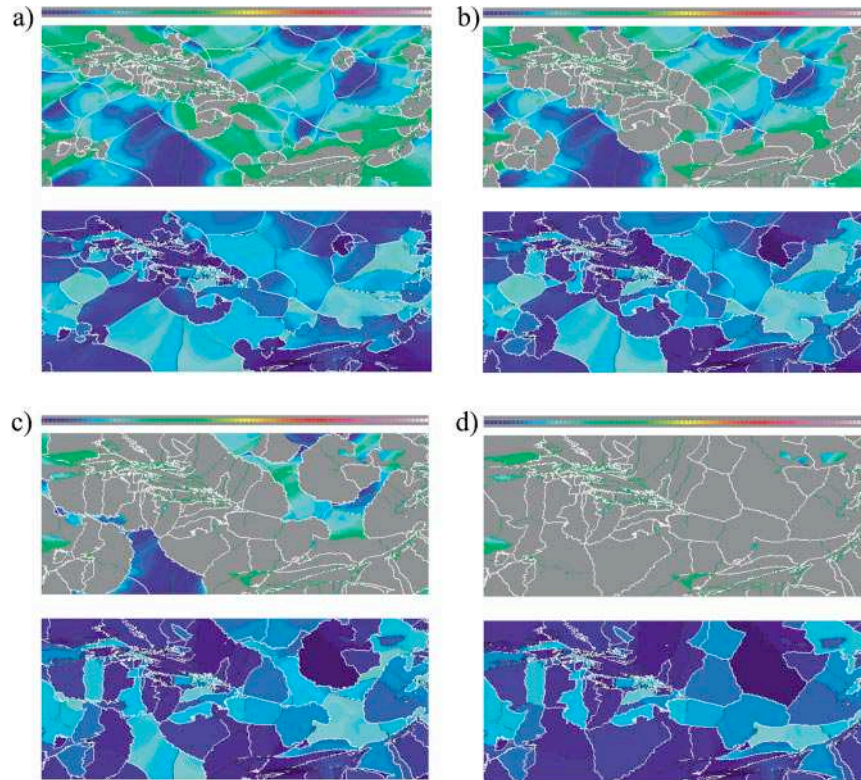


**Figure 5** Consecutive stages of a two-dimensional simulation of primary static recrystallization in a deformed aluminum polycrystal on the basis of crystal plasticity finite element starting data. The figure shows the change in dislocation density (*top*) and microtexture (*bottom*) as a function of the annealing time during isothermal recrystallization. The texture is given in terms of the magnitude of the Rodriguez orientation vector using the cube component as reference. The *gray areas* in the upper figures indicate a stored dislocation density of zero, i.e., these areas are recrystallized. The *heavy white lines* indicate grain boundaries with misorientations above  $15^\circ$  irrespective of the rotation axis. The *thin green lines* indicate misorientations between  $5^\circ$  and  $15^\circ$  irrespective of the rotation axis. The simulation parameters: 800 K; thermodynamic instability criterion, site-saturated spontaneous nucleation in cells with at least 50% of the maximum occurring dislocation density (threshold value); kinetic instability criterion for further growth of such spontaneous nuclei, misorientation above  $15^\circ$ ; activation energy of the grain boundary mobility, 1.46 eV; pre-exponential factor of the grain boundary mobility,  $m_0 = 8.3 \times 10^{-3} \text{ m}^3/(\text{N s})$ ; mesh size of the cellular automaton grid (scaling length),  $\lambda_m = 61.9 \text{ } \mu\text{m}$ .

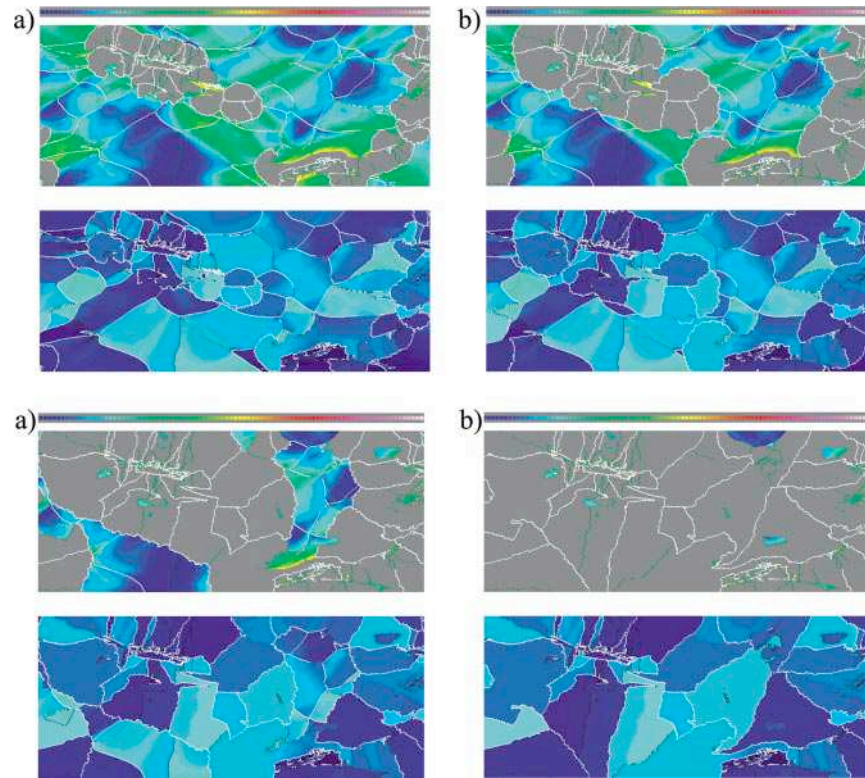


**Figure 6** Parameters such as in Figure 5, but site-saturated spontaneous nucleation occurred in all cells with at least 60% of the maximum occurring dislocation density.

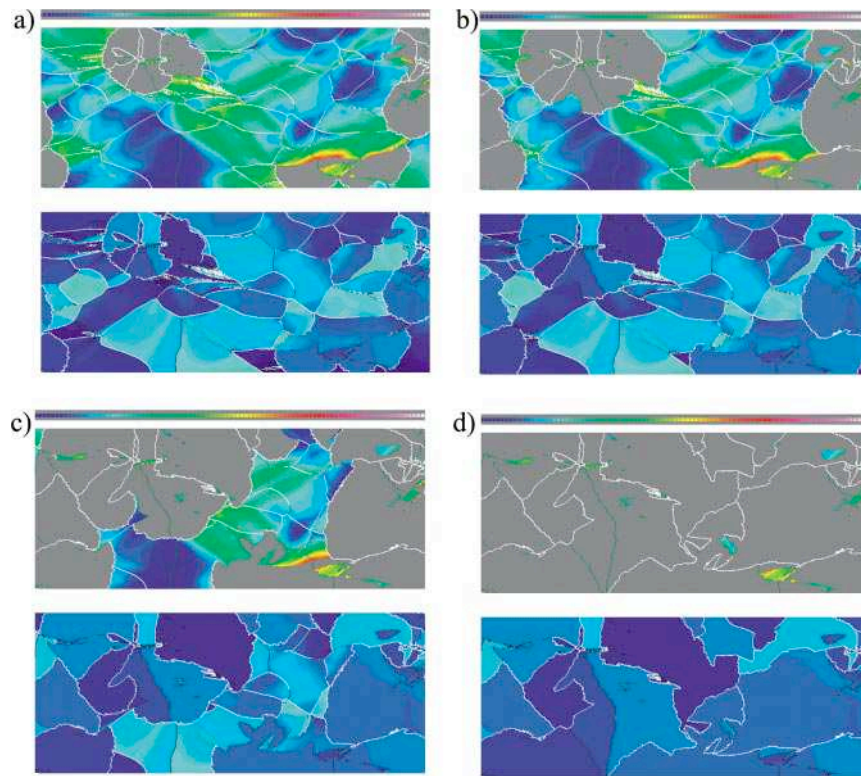


**Figure 7** Parameters such as in Figure 5, but site-saturated spontaneous nucleation occurred in all cells with at least 70% of the maximum occurring dislocation density.

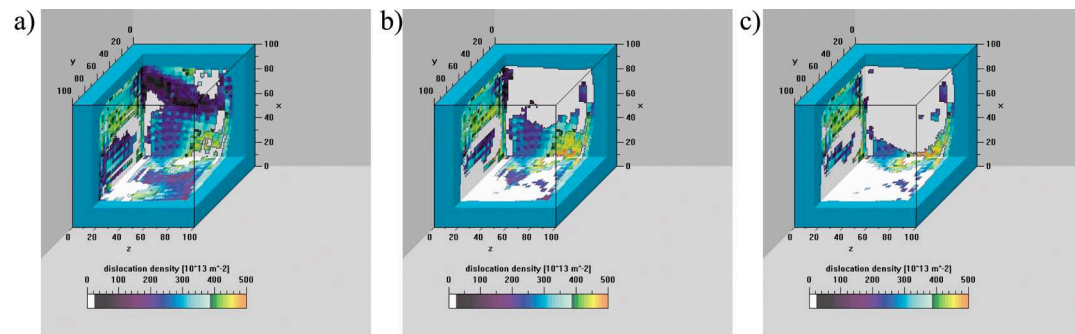


**Figure 11** Change in dislocation density during recrystallization (800 K). The color scale indicates the dislocation density of each lattice point in units of  $10^{13} \text{ m}^{-2}$ . The *white areas* are recrystallized. The surrounding *blue area* indicates the continuum material in which the grain is embedded. (a) 9% of the entire sample recrystallized, 32.1 s; (b) 19% of the entire sample recrystallized, 45.0 s; (c) 29.4% of the entire sample recrystallized, 56.3 s.

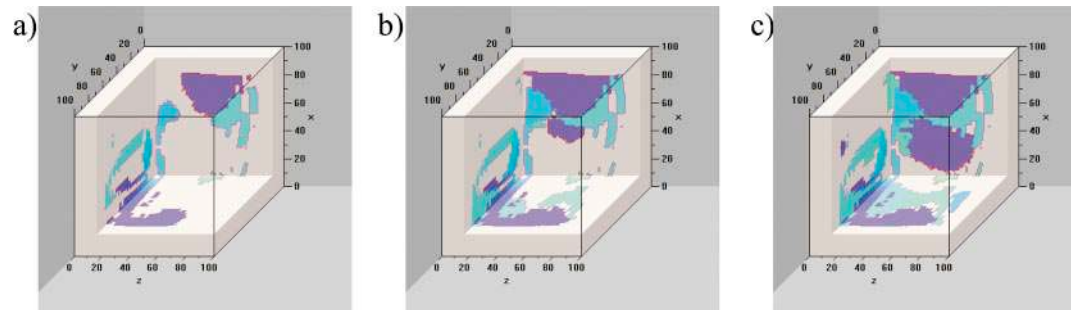


**Figure 12** Topology of the evolving nuclei of the microstructure given in Figure 11 without coloring the as-deformed volume. All newly recrystallized grains are colored indicating their crystal orientation. The non-recrystallized material and the continuum surrounding the grain are *white*. Sample recrystallization percents same as in Figure 11.